DOCTORAL THESIS

Thesis Title

Author:

Ana ANDRES-ARROYO

Supervisor:

Dr. First LAST

A thesis submitted in fulfilment of the requirements for the degree of

Doctor of Philosophy

School of Physics, Faculty of Science

July 2018

Dedicated to someone.

"Fancy Quote"

Author

Abstract

School of Physics, Faculty of Science, UNSW Australia

Doctor of Philosophy

Thesis Title

by Ana ANDRES-ARROYO

Write your abstract here .

Acknowledgements

The acknowledgements and the people to thank go here, don't forget to include your project advisor. . .

Contents

x

List of Figures

Abbreviations

2D   Two-**D**imensional

3D   Three-**D**imensional

Physical Constants

Speed of Light $\quad\quad\quad\quad c \quad = \quad$ 2.997 924 58 $\times 10^8$ ms^{-S} (exact)

Constant Name $\quad$ Symbol $\quad = \quad$ Constant Value (with units)

Symbols

f	focal length	mm or cm
H	heating	K/W
I	intensity	a.u.
k	trap stiffness	pN/μm/mW
n	refractive index	—
P	power	mW
T	temperature	°C or K
ε	permittivity	???
κ	trap stiffness	pN/μm/mW
λ	wavelength	nm
μ	permeability	???
σ	cross section	???
θ	tilt angle	degrees or radians

Chapter 1

Introduction

1.1 Section title

Always put labelthesection after each section so the page headers work. [1]

This is a test.

1.2 Compiling instructions

1. make the main file the masted document: options -¿ make current file masted document

2. Quick build from anywhere (because it quick builds from the master document

3. BibTex from the chapter file (disable the master document option for this and do it from "normal mode")

4. Quick build 3 times (from the master document): 1 for the text, 2 for the references and labels, 3 for the bibliography backreferencing.

1.3 References

[1] D. Selmeczi, S. F. Tolic-Norrelykke, E. Schaffer, P. H. Hagedorn, S. Mosler, K. Berg-Sorensen, N. B. Larsen, and H. Flyvbjerg. Brownian motion after einstein and smoluchowski: Some new applications and new experiments. *Acta Physica Polonica B*, 38(8):2407–2431, 2007. Cited in pages: 2

₁ # Chapter 2

Fourier transform as measurement of radial velocity

This chapter will introduce a new method to measure the radial velocity. We will study, in Fourier transform, the features of a signal shift from time domain to frequency domain. The results will be applied to measuring non-deformed spectral line shifts. We will then extend the study to measuring the apparent radial velocity shift due to line profile deformation.

2.1 Fourier transform as measurement of line shift

2.1.1 Translation property of Fourier transform

Translation is also known as time shifting, as Fourier transform usually deals with time sequence signals. In this chapter, we use time domain and frequency domain to differentiate the signal before and after Fourier transform, regardless of the nature of the signal.

Let $h(x)$ be a signal $f(x)$ delayed (or shifted) by x_0:

$$h(x) = f(x - x_0). \tag{2.1}$$

In the frequency domain, we have

$$\hat{h}(\xi) = e^{-2\pi i x_0 \xi} \hat{f}(\xi), \tag{2.2}$$

where the circumflex denotes Fourier transform of a function. This formula shows that $\hat{h}(\xi)$ and $\hat{f}(\xi)$ differ by a frequency dependent phase angle

$$\Delta\phi(\xi) = -2\pi x_0 \xi \tag{2.3}$$

while the power spectral density remains the same (as $\mid e^{-2\pi i x_0 \xi} \mid^2 = 1$).

2.1.2 Intuitive explanation

Although the translation property of Fourier transform can be mathematically proven, I provide a more intuitive explanation in the following.

By definition

$$\hat{f}(\xi) = \int_{-\infty}^{\infty} f(x) e^{-2\pi i x \xi} dx, \tag{2.4}$$

Fourier transform decomposes the function $f(x)$ into frequency representations $\hat{f}(\xi)$, such that the function itself can be expressed as the sum of *all* orthogonal basis $e^{2\pi i x \xi}$, which is also known as the inverse Fourier transform:

$$f(x) = \int_{-\infty}^{\infty} \hat{f}(\xi)e^{2\pi i x \xi}d\xi. \tag{2.5}$$

Note that shifting $f(x)$ by x_0 is equivalent to shifting *all* the orthogonal basis by x_0, which becomes $e^{2\pi i(x-x_0)\xi}$. This is how the extra term $e^{-2\pi i x_0 \xi}$ comes along – it contributes to the phase difference [1].

The fact that the power spectrum density remains the same can also be viewed intuitively – shifting the signal as a whole doesn't add or remove any frequency information. In other words, the composition of the signal doesn't change.

2.1.3   How to use

From Eq. 2.3, we could see that the phase shift $\Delta\phi(\xi)$ is proportional to the frequency ξ with the constant gradient

$$\text{slope} = \frac{d(\Delta\phi)}{d\xi} = -2\pi x_0 \tag{2.6}$$

In practice, obtaining the slope is as easy as fitting the measured $\Delta\phi(\xi)$ and ξ with linear regression model (Fig. 2.1). Therefore, the shift can be calculated as

$$x_0 = -\frac{\text{slope}}{2\pi} \tag{2.7}$$

Analogous to the definition of power spectral density, we call $\phi(\xi)$ the phase spectral density and hence $\Delta\phi(\xi)$ the differential phase spectral density.

Concluding remarks   Fourier transform bridges the signal shift (or delay) in the time domain and the phase shift in the frequency domain, and hence the phase shift can be used to estimate signal shift by Fourier transform.

---

[1]For a simplified vision bridging a shift of the signal in the time domain and a phase difference in the frequency domain, imagine any real continuous function is a sum of sines and cosines. Changing the phase angle in the sines and cosines results in shifts in the function.
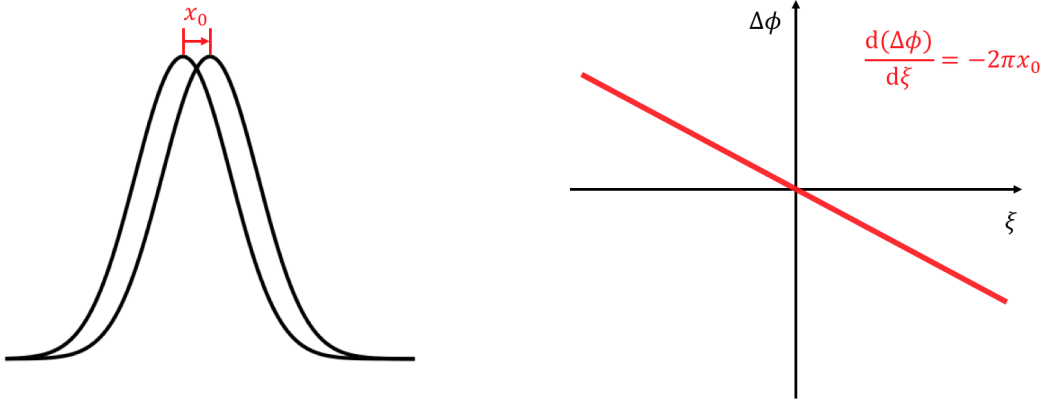
Fig. 2.1: The left panel shows a signal (or a spectral line profile in the following context) shifted by an amount x_0. The right panel is the differential phase spectral density diagram (i.e. differential phase spectrum). The model shows a perfectly linear correlation between $\Delta\phi(\xi)$ and ξ with the constant slope $-2\pi x_0$.

2.1.4 Sanity check

We will perform a sanity check to see if we could correctly recover the shifts of a line profile by analysing the phase shift through Fourier transform.

First of all, we generate a spectral line profile based on the cross-correlation function of observed HARPS spectrum with the software SOAP 2.0. A tiny amount of noise (S/N=10,000) has been injected in the line profiles. We then apply 100 radial velocity shifts evenly spaced between 0 and 10 m/s (Fig. 2.2). The Fourier transform of the 100 spectral line profiles divides the information into two parts: (1) the power spectra (Fig. 2.3a) and (2) the phase spectra, from which we obtain the differential phase spectra relative to the non-shifted line profile (Fig. 2.3b). We notice that most of the information are concentrated in the lower frequency range in the power spectrum, and as expected, the differential phase spectra are linear by eye [2]. The slopes of the differential phase spectra indicate the amount of shifts relative to the non-shifted line profile. At last we calculate the radial velocity shifts using two methods: (1) RV_{FT} from Eq. 2.7 and (2) RV_{Gaussian} traditionally the line centroid by fitting a Gaussian profile, both compared with the input line shift (Fig. 2.4). The root mean square of the residual are $rms_{\mathrm{FT}} = 0.13$ m/s and $rms_{\mathrm{Gaussian}} = 0.09$ m/s respectively, indicating very consistent radial velocities. Note that rms_{FT} is slightly larger than rms_{Gaussian}. This is because we only use part of the information from the line profile – the lower frequency section of the differential phase spectra. In fact, higher frequency range becomes useless as the

---

[2] The slight deviation from linearity may come from the noise that we injected.

(a) Line profile (stacked)
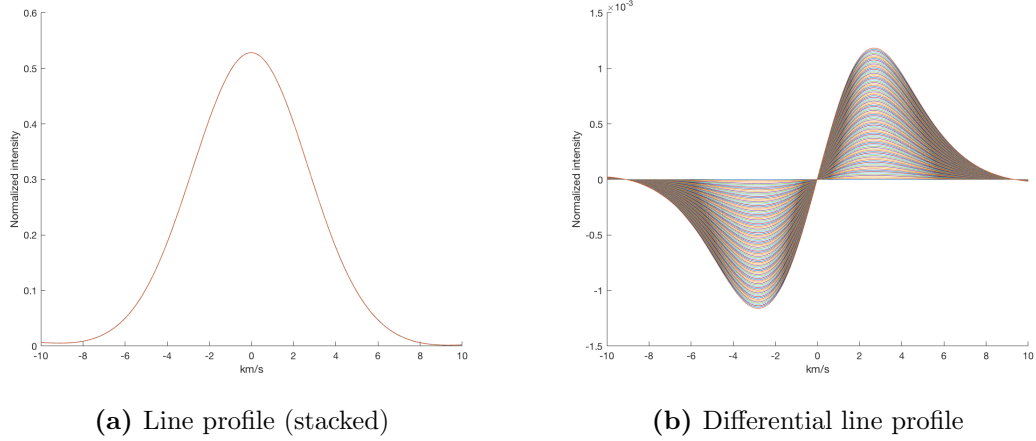

(b) Differential line profile

Fig. 2.2: Shifted line profile. Note that for demonstration purpose, noise is not included in this differential line profile plot, otherwise the pattern of the differential will be overwhelmed by noise.
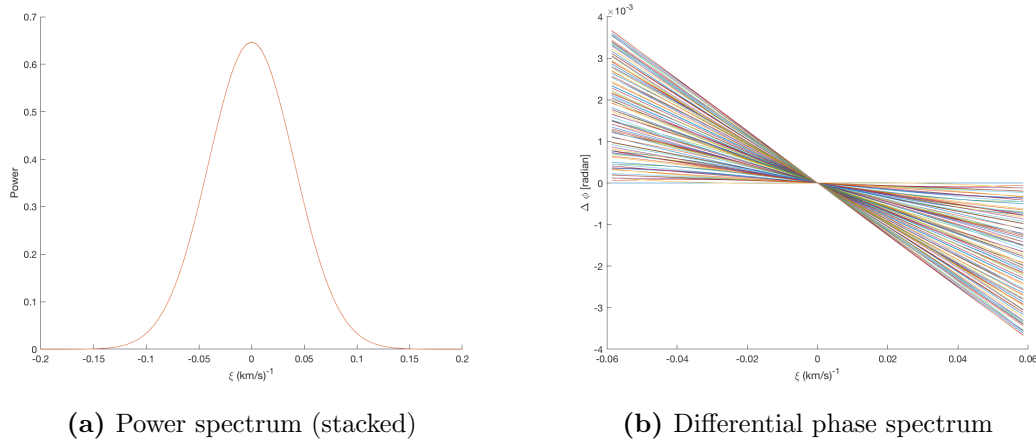

(a) Power spectrum (stacked)

(b) Differential phase spectrum

Fig. 2.3: Fourier transform of shifted line profile divides the information into the power spectrum and the (differential) phase spectrum. For a line shift in time domain, it is translated into phase shift in frequency domain, and shows linearity in the (differential) phase spectrum.

interpretation of Fourier transform in high frequencies is dominated by noise and does not represent the intrinsic shift of the line profile any more. As a result, linearity of phase spectrum breaks down in higher frequencies. The range of "useful" frequencies will depend on the amount of noise (i.e. S/N).

Concluding remarks The sanity check has passed – we have successfully recovered the radial velocity shifts of the line profile by the phase shift analysis in Fourier transform. We view this method as an alternative to the traditional ways of obtaining the radial velocity under the circumstances where no line deformation is present.
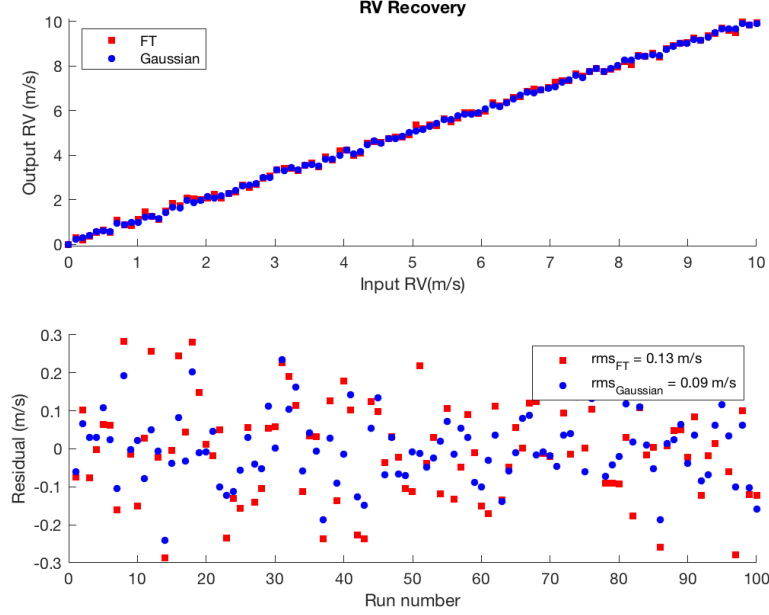
Fig. 2.4: Radial velocity recovery of line shifts

In a broader context, we expect this method will be applicable to measuring shifts of any pattern, and it can be extended to higher dimensions. In this thesis, we primarily use it to detect radial velocity shifts of spectral line profile.

2.2 Fourier transform as measurement of line deformation

2.2.1 Theory

With this new method to detect radial velocities, we are eager to test out, its response to the apparent radial velocity due to spectral line deformation. In § 2.1, the same shift x_0 applies to *all* the basis frequencies. This is a very important premise so that we could make use of the linearity of the differential phase spectral density $\Delta\phi(\xi)$ (see Eq. 2.3). In the case of line deformation due to stellar variability, x_0 becomes frequency dependent [3]. That is to say, basis functions of different frequencies would shift by different amounts, resulting in shape changes (e.g. skewness) in the line profile. Therefore we modify the

---

[3]excluding the case where the result of a line deformation is exactly the same as a line shift, as this becomes indistinguishable by any means

translation property of Fourier transform by rewriting x_0 as $x_0(\xi)$ in Eq. 2.3:

$$\Delta\phi(\xi) = -2\pi x_0(\xi)\xi. \tag{2.8}$$

As a result, the local gradient of the differential phase spectrum becomes

$$\frac{\mathrm{d}(\Delta\phi)}{\mathrm{d}\xi} = -2\pi(x_0 + \frac{\mathrm{d}x_0}{\mathrm{d}\xi}), \tag{2.9}$$

which degenerates to Eq. 2.6 when x_0 is a constant as in the case of line shifts. Note that the dependency of ξ has been taken out from $\Delta\phi(\xi)$ and $x_0(\xi)$ in writing the differential equation above.

In principle, we could numerically solve this differential equation based on the measured local gradient $\mathrm{d}(\Delta\phi)/\mathrm{d}\xi$ to obtain $x_0(\xi)$. As a simplistic approach, if $x_0(\xi)$ changes with ξ slowly within a certain frequency range, we can make the approximations that $x_0 \sim \mathrm{const}$ and $\mathrm{d}x_0/\mathrm{d}\xi \sim 0$. With this, Eq. 2.9 converges back to Eq. 2.6.

2.2.2 SOAP Simulations

With SOAP 2.0, we inject three spots with different longitudes, latitudes and sizes (Table 2.1) and generate 100 of the cross-correlation functions of the deformed line profiles evenly sampled throughout the rotation period of the star (Fig. 2.5). We then take the same approach as if we dealt with line shifts in § 2.1.

	Longitude	Latitude	Size in disk area percentage
Spot 1	174°	-14°	0.18%
Spot 2	288°	74°	0.40%
Spot 3	51°	52°	0.50%

Table 2.1: Spot configurations

If we compare the differential phase spectra in Fig. 2.3 and Fig. 2.6, it is quite obvious that the differential phase spectrum of a deformed line profile is no longer linear due to the x_0 dependency on ξ, as we discussed in § 2.2.1. Nevertheless, applying the local linear approximation will provide a radial velocity shift for that frequency range. We will primarily use the lower frequency range (from -0.06 to 0.06 $(\mathrm{km/s})^{-1}$ in this case) for the reasons that it is where information is mostly concentrated and that it is less noise-sensitive.
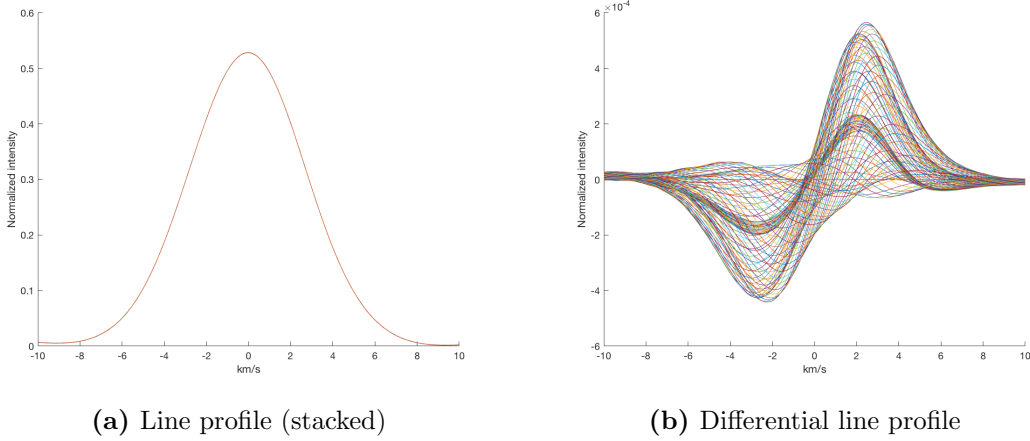
(a) Line profile (stacked)

(b) Differential line profile

Fig. 2.5: Deformed line profile. Note that noise is not included in this differential line profile plot for the same reason.
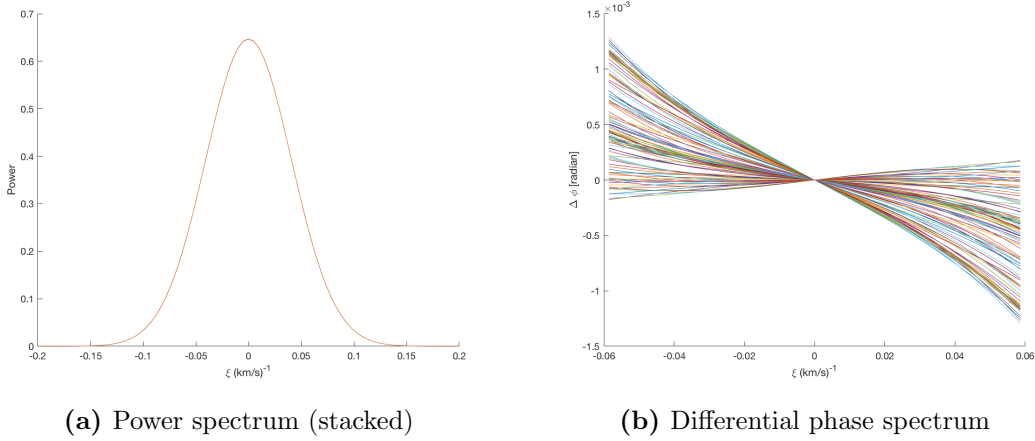

(a) Power spectrum (stacked)

(b) Differential phase spectrum

Fig. 2.6: Fourier transform of deformed line profile.

We find, to our surprise, that RV_{FT} is not only linearly correlated with RV_{Gaussian}, but also comes with a non-unity slope $k \sim 0.84$ (Fig. 2.7). The non-zero slope indicates without line shift, the intrinsic line deformation alone disguises itself so well that even analysing the radial velocity shift by frequency has its limitations. However, it does turn out that frequency analysis in the lower frequency bases are less sensitive to line deformation. In this particular circumstance, the region that we study has a frequency modulation of $| \xi | < 0.06 \ (\mathrm{km/s})^{-1}$, which is equivalent to oscillations of wavelengths $\lambda = 1/ | \xi | > 16$ km/s. These are indeed lower frequency modes less effectively modulated by the higher frequency deformations, as shown in the differential line profile in Fig. 2.5b. In addition, the slope k will change depending on the frequency range in which the linear regression model is applied. For example, if we select the higher frequency range in the differential phase spectrum, we will expect larger RV_{FT} and hence a larger k in general.
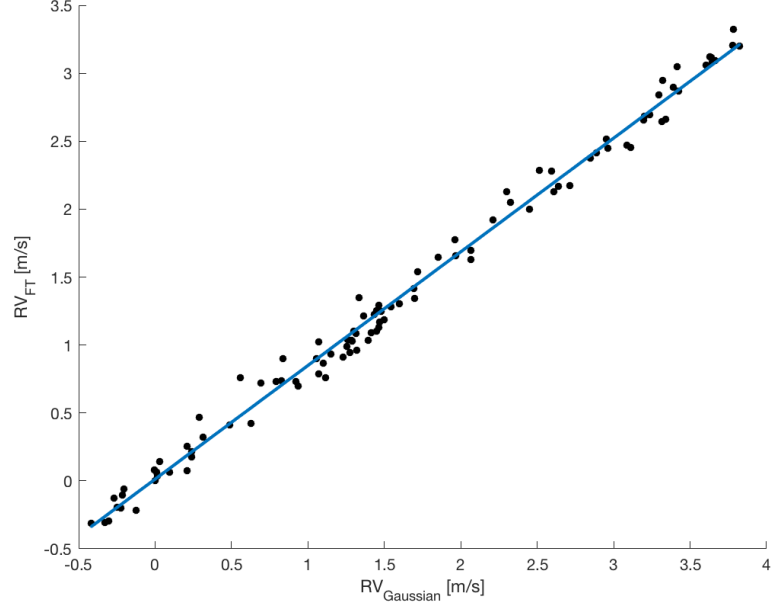
Fig. 2.7: $RV_{\mathrm{FT}} \sim k \cdot RV_{\mathrm{Gaussian}}$ $(k < 1)$

2.2.3 Jitter model

We have learnt in § 2.1 that RV_{FT} and RV_{Gaussian} demonstrate basically the same response to radial velocity shifts. We have also learnt in this section (§ 2.2) that RV_{FT} in the lower frequency range is less sensitive to line deformation than RV_{Gaussian}, scaled by the factor k. Therefore, we write the following measurable quantities – RV_{FT} and RV_{Gaussian} – as the sum of corresponding contributions from the planet(s) and stellar variability (a.k.a jitter):

$$RV_{\mathrm{Gaussian}} = RV_{\mathrm{planet}} + RV_{\mathrm{jitter}} \qquad (2.10)$$

and

$$RV_{\mathrm{FT}} = RV_{\mathrm{planet}} + k \cdot RV_{\mathrm{jitter}}. \qquad (2.11)$$

Subtracting one from the other cancels out RV_{planet} and gives

$$\Delta RV = (1 - k) \cdot RV_{\mathrm{jitter}} \qquad (2.12)$$

where $\Delta RV = RV_{\mathrm{Gaussian}} - RV_{\mathrm{FT}}$. Rearranging yields

$$RV_{\mathrm{jitter}} = \alpha \cdot \Delta RV \qquad (2.13)$$

where $\alpha = 1/(1-k)$ is a scaling factor.

2.2.4   Sanity check

We will again perform a sanity check to see if we could correctly recover the jitter based on our jitter model (Eq. 2.13).

To start with, we generate 200 deformed line profiles (in the form of cross-correlation functions) with SOAP 2.0. All the configurations are the same as §2.2.2 except that they are evenly sampled throughout two rotation periods. The jitter amplitude is roughly 2 m/s. In addition, each line profile is further shifted by an amount RV_{planet}, of which the amplitude

$$A_{\mathrm{planet}} = 2 \text{ m/s}$$

and the planetary orbital frequency to stellar rotation frequency ratio

$$\frac{\nu_{\mathrm{orb}}}{\nu_{\mathrm{rot}}} = \frac{P_{\mathrm{rot}}}{P_{\mathrm{orb}}} = 0.7.$$

In fact, the RV_{planet} configuration shouldn't matter much because it will be mostly cancelled out in the jitter model. We then obtain two sets of radial velocities: RV_{Gaussian} and RV_{FT}, as seen in the upper panel of Fig. 2.8. As we know the amount of input jitter in our simulation, we simply scale up ΔRV by a parameter α to match the input jitter (dashed line in middle panel). The jitter model (black dots in middle panel) becomes more scattered as $\alpha \gg 1$. As a result, a moving average modulated by a Gaussian kernel is implemented to smooth out the data (solid line in middle panel).

To comment on the performance, we compare the rms of the input jitter rms_{jitter} and the rms of the residual between the input jitter and the model jitter rms_{residual}. The former can be treated as the scatter after fitting the correct planet(s) without jitter correction, while the latter treated as the scatter after the additional jitter is removed. The rms is reduced from $rms_{\mathrm{jitter}} = 1.22$ m/s to $rms_{\mathrm{residual}} = 0.70$ m/s, which is crucial in enhancing the detection of planets with radial velocities of sub-m/s amplitudes. However, we should also note that there are systematic differences between the input jitter and our model jitter (i.e. the residual sorts of repeats itself in the two stellar rotation periods). We should be aware that while removing the stellar variability contribution from the data, it may also add in some remnant features.
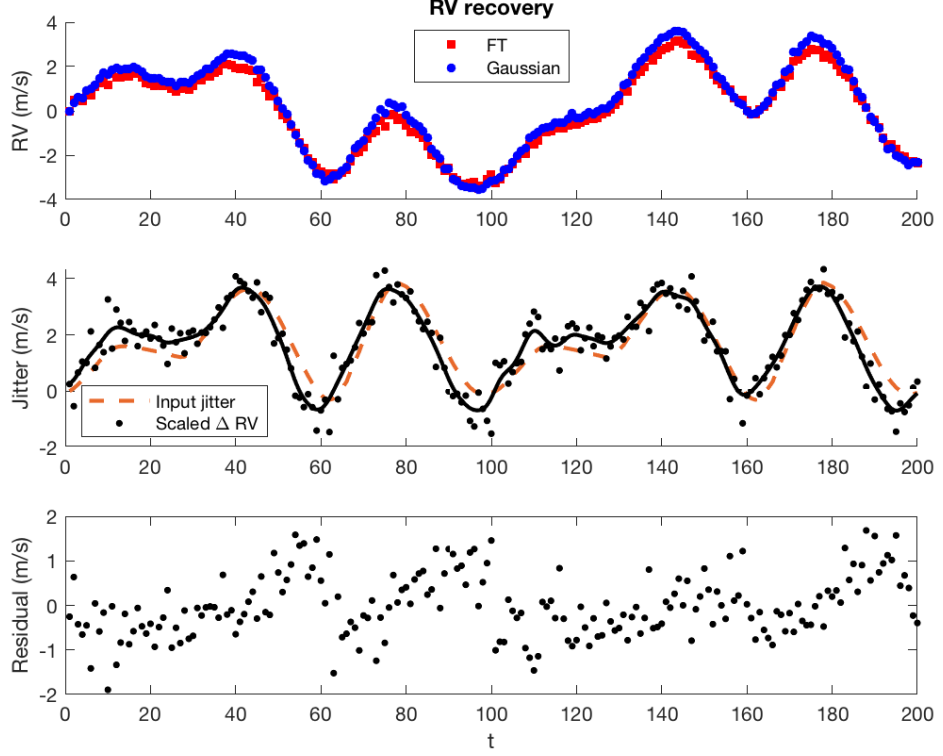
Fig. 2.8: Construct jitter model from simulation data.

2.2.5 End-to-end Simulations

Unless we are sure of a null-planetary system where $RV_{\text{planet}} = 0$ and from Eq. 2.10 and Eq. 2.11 we obtain

$$k = RV_{\text{jitter}}/RV_{\text{Gaussian}}, \tag{2.14}$$

normally k cannot be directly calculated, so neither can α be. However, we could substitute the jitter model (Eq. 2.13) into Eq. 2.10, such that

$$RV_{\text{Gaussian}} = RV_{\text{planet}} + \alpha \cdot \Delta RV \tag{2.15}$$

where RV_{planet} is parametrised by Keplerian orbit(s) and both RV_{Gaussian} and ΔRV are measurable.

The tests are divided into two groups for comparison:

1. Fit RV_{Gaussian} by Keplerian orbit alone;

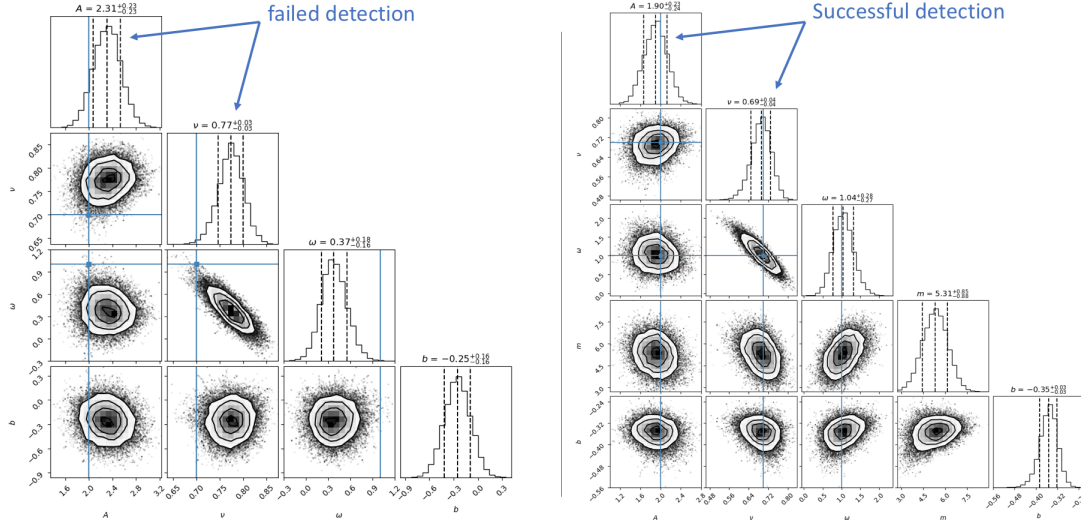2. Fit RV_{Gaussian} by Keplerian orbit + jitter model (i.e. $\alpha \cdot \Delta RV$).

Fig. 2.9: Corner plots of MCMC. Theses are two examples of the output of MCMC: no jitter correction on the left and with jitter correction on the right. The input parameters are highlighted in the blue solid line. The three dashed lines of each histogram indicate the median and 1σ on both sides. On the left panel both blue lines of A and ν are outside the 1σ region, therefore it counts as a "failed detection"; on the right panel, it counts as a successful detection within 1σ.

The injected planet has the same parameter settings as in §2.2.4, i.e. circular orbit with amplitude $A = 2$ m/s, orbital frequency ratio $\nu = 0.7$ and initial phase $\omega = 1$ rad. We will compare which group recovers the planet parameters better.

To better simulate the real observations, 40 data samples out of 200 from the two rotation periods are randomly selected. The fitting is achieved by running MCMC to maximise the log-likelihood function given the model. For the simulation, each radial velocity data is equally weighted (as they have the same S/N). It is defined if the input parameter lies within 1σ errorbar of the output parameter, it counts as a successful detection.

For demonstration, we show one of the outputs in corner plots (Fig. 2.9) and the corresponding radial velocity fitting (Fig. 2.10). The corner plot visually shows the how the walkers explore the parameter space and their distribution. The histogram gives an example explaining how a "successful detection" is qualified. The radial velocity fitting plot demonstrates an example that implementing the jitter model effectively accounts for the spurious signals in the raw radial velocity data, reducing the rms from 1.14 m/s to 0.55 m/s.
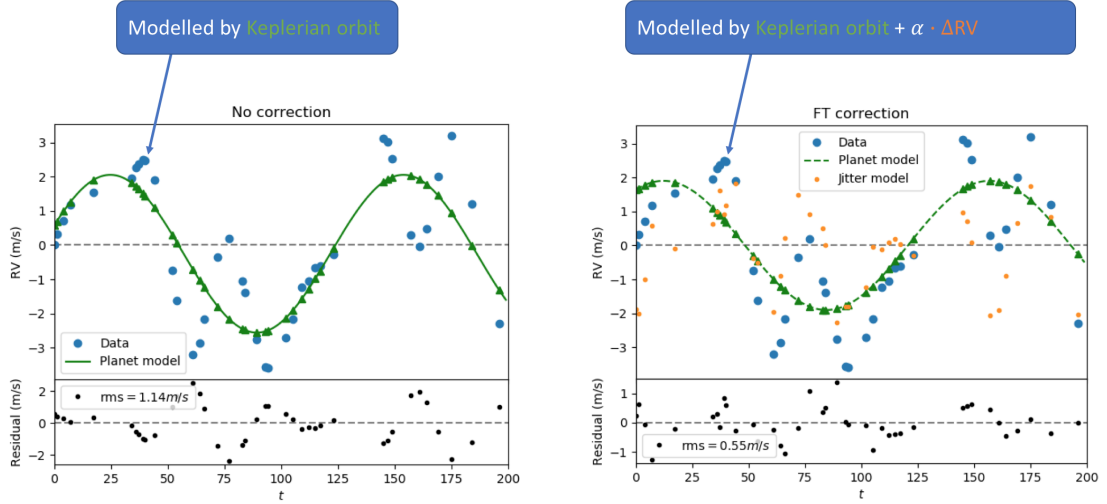
Fig. 2.10: Radial velocity fitting. Theses are two fittings that comes out from the MCMC corner plots in Fig. 2.9. On the left panel without jitter correction, we can see that the input jitter increases the scatter of the raw radial velocities, resulting in an overestimated amplitude A; while on the right panel with jitter correction, the additional input jitter is accounted for by the jitter model.

In the end, we run 100 trails for the end-to-end simulation. The random differences among these 100 trails come from:

- photon noise given the S/N;

- randomly selected 40 samplings in the 200 line profiles.

It turns out that in 46% of the 100 trails are successful detections for both A and ν when we apply the jitter correction model, while this percentage is only 11% without jitter correction. In more detail, Fig. 2.11 shows that with jitter correction (in red), both of the amplitude and orbital frequency ratio tend to be underestimated, which is shown opposite for the results without correction (in blue). Moreover, the jitter corrected parameters are better constrained (i.e. with narrower distributions) and performs much better in ν than without correction. While it is tempting to say the correct answer is more likely in between the results from these two fittings, we would need more tests to conclude.
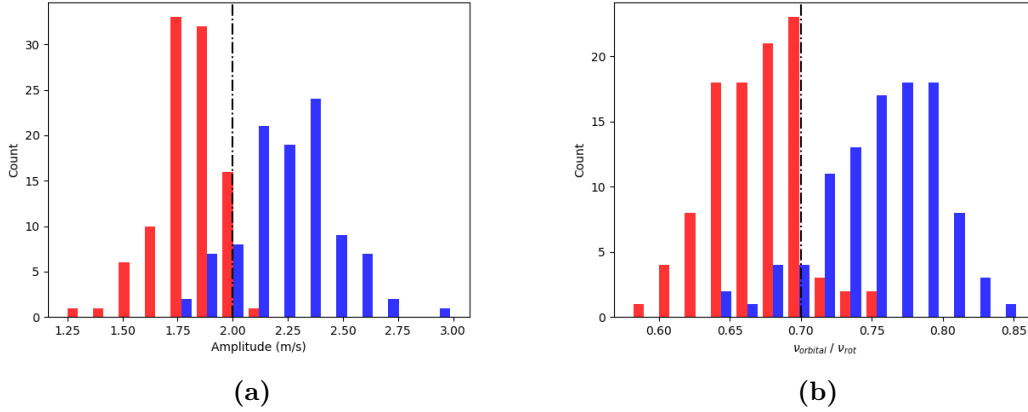
(a)

(b)

Fig. 2.11: Distribution of recovered parameters. The red are results of jitter correction by Fourier transform; The blue are results of no jitter correction.

2.3 Fourier transform with real observations

2.3.1 HD189733: Rossiter–McLaughlin effect as jitter

HD189733 is a well studied binary star system. The main star HD189733 A is known to host a gas giant exoplanet HD189733 b, first detected by transits (reference...) and later by Doppler spectroscopy (references...). It was also the first exoplanet transit observed in X-ray (references...).

We choose this target for the following reasons:

- The exoplanet is well confirmed;

- The host star is bright enough: $m_v = 7.66$

- The gas giant causes a prominent apparent radial velocity while it transits ($\sim$ 40 m/s) due to Rossiter–McLaughlin effect.

We treat as if it were an "active" star with one big dark starspot, as the Rossiter–McLaughlin effect causes the line profile deformed in a similar manner that a starspot would do (Fig. 2.12). We would see if our jitter model can account for the radial velocity variation from Rossiter–McLaughlin effect.

The procedure is rather standardized. Both RV_{Gaussian} and RV_{FT} are calculated from the HARPS cross-correlation functions of the spectra. $\Delta RV = RV_{\mathrm{Gaussian}} - RV_{\mathrm{FT}}$
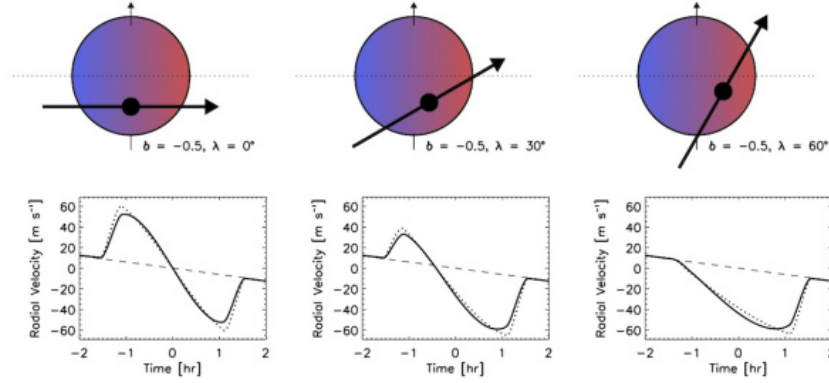
Fig. 2.12: Demo: Rossiter–McLaughlin effect (reference...). It is a apparent radial velocity change of the parent star due to an eclipsing binary (whether star or planet) that breaks the observed flux symmetry in the stellar photosphere, resulting in imbalanced redshift and blueshift. It shows in this plot three different star-planet alignments that causes three corresponding different shapes of radial velocity curve, and hence the radial velocity curve sheds information on the geometry of the alignment.

are then smoothed by a Gaussian filter (Fig.2.13). The prototype of the Rossiter–McLaughlin radial velocity curve is already identifiable in ΔRV of the lower panel.

To extract the Rossiter–McLaughlin radial velocity curve, a linear trend is fitted to account for the other binary star. After the linear trend is removed, it is treated as jitter and modelled by $\alpha \cdot \Delta RV$ (Fig. 2.14). Note that the errorbars of the jitter model also becomes a factor of α ($\alpha \gg 1$) larger; however, the model itself shows a descent approximation of the Rossiter–McLaughlin radial velocity curve. The peak of the "jitter" is reduced from ~ 40 m/s to ~ 10 m/s.

Remarks The effective length of the smoothing kernel should be carefully chosen. In this case, it's chosen most effective within roughly one neighbouring data point on both size. While mitigating the effect of noise (especially for relatively lower S/N data outside the transits), to which the Fourier transform is sensitive, it also smears the drastic velocity change when the planet ingresses and egresses the stellar disk. To solve this awkward situation, an adaptive (i.e. S/N dependent) effective length of the smoothing kernel may be used.
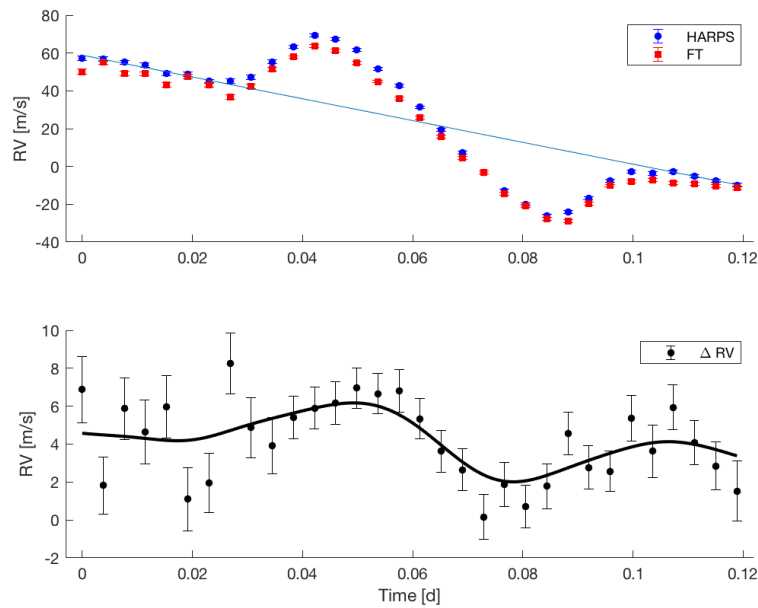
2.3.2 Examples 2

2.3.3 Example 3

Fig. 2.13: From RV_{Gaussian} and RV_{FT} to ΔRV. The scattered ΔRV are smoothed by applying a moving average with a Gaussian filter and further weighted based on the size of errorbar.
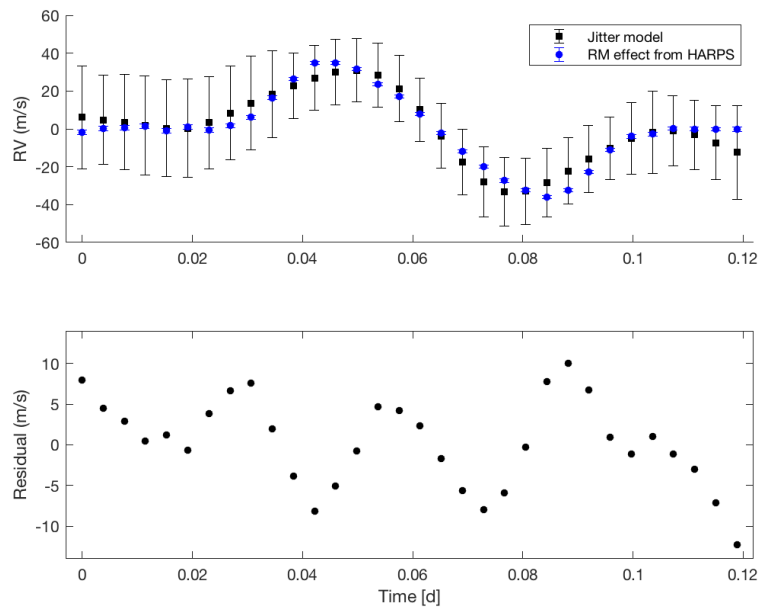

Fig. 2.14: Rossiter–McLaughlin effect as jitter fitted with the jitter model.

A float barrier will stop figures from going beyond this point. They are handy to make sure they don't go into the next section.

2.4   References

[1] D. Selmeczi, S. F. Tolic-Norrelykke, E. Schaffer, P. H. Hagedorn, S. Mosler, K. Berg-Sorensen, N. B. Larsen, and H. Flyvbjerg. Brownian motion after einstein and smoluchowski: Some new applications and new experiments. *Acta Physica Polonica B*, 38(8):2407–2431, 2007. Cited in pages: